Available online at www.sciencedirect.com
SCIENCE DIRECT®
C. R. Mecanique 331 (2003) 17–24
COMPTES RENDUS MECANIQUE

Experimental and computational visualization of the flow field in a thermoacoustic stack

Visualisation expérimentale et numérique du champ de vitesse dans un réfrigérateur thermoacoustique

Philippe Blanc-Benon [a], Etienne Besnoin [b], Omar Knio [b]

[a] *Centre acoustique, LFMA UMR CNRS 5509, École centrale de Lyon, 69134 Écully cedex, France*
[b] *Department of Mechanical Engineering, The Johns Hopkins University, Baltimore, MD 21218, USA*

Received 24 October 2002; accepted 19 November 2002

Presented by Geneviève Comte-Bellot

Abstract

The oscillating flow field in a thermoacoustic stack is visualized experimentally using PIV measurements, and computationally using results of low-Mach-number simulations. The experiments and computations are performed under similar conditions. Results are obtained for two distinct configurations, involving thin and thick stack plates. In the first case, the flow field around the edge of the stack exhibits elongated vorticity layers, while in the latter it is dominated by the shedding and impingement of concentrated vortices. A close agreement between experimental and computational results is found, thus providing strong support for both approaches and further predictions. ***To cite this article: P. Blanc-Benon et al., C. R. Mecanique 331 (2003).***

Résumé

L'écoulement oscillant autour de l'empilement de plaques d'un réfrigérateur thermoacoustique est visualisé expérimentalement avec une technique PIV et numériquement en utilisant des simulations basées sur un modèle d'écoulement à faible nombre de Mach. Les conditions d'expérience et de simulation sont similaires. Les résultats sont obtenus pour deux configurations distinctes, respectivement des plaques épaisses et des plaques fines. Dans le deuxième cas, l'écoulement autour des extrémités est caractérisé par des couches de vorticité étirées, alors qu'avec des plaques épaisses l'écoulement est dominé par les oscillations de tourbillons denses. Les résultats obtenus expérimentalement et numériquement sont similaires, et renforcent la validité des deux méthodes. ***Pour citer cet article : P. Blanc-Benon et al., C. R. Mecanique 331 (2003).***

Keywords: Heat transfer; Thermoacoustics; Oscillatory flow; PIV; Simulation

Mots-clés : Transfers thermiques ; Thermoacoustique ; Écoulement oscillant ; PIV ; Simulation

E-mail addresses: philippe.blanc-benon@ec-lyon.fr (P. Blanc-Benon), etienne@jhu.edu (E. Besnoin), knio@jhu.edu (O. Knio).

1631-0721/03/$ – see front matter
doi:10.1016/S1631-0721(02)00002-5

Version française abrégée

Le fonctionnement d'un réfrigérateur thermoacoustique [1,2] est basé sur l'effet thermoacoustique, qui induit un flux de chaleur d'une extrémité vers l'autre d'un empilement de plaques, appellé aussi stack, placé dans un tube de résonance (voir Fig. 1). Des échangeurs de chaleur placés de chaque côté de l'empilement permettent d'exploiter ce flux de chaleur et de maintenir un cycle de réfrigération grâce à l'onde stationnaire existant dans le tube. L'observation de la présence de vortex [3–7] autour des extrémités des plaques de l'empilement a mis en évidence la nécessité de comprendre l'impact de la géométrie et des conditions de fonctionnement sur l'écoulement et par conséquent sur les performances du système thermodynamique.

Cette étude présente les résultats de visualisations expérimentales et numériques de l'écoulement autour de l'empilement de plaques d'un réfrigérateur thermoacoustique obtenues dans des conditions similaires. Les visualisations sont obtenues pour de faibles amplitudes de l'onde acoustique, avec des plaques fines et épaisses comparées à l'épaisseur de la couche limite visqueuse. La technique utilisée pour les mesures expérimentales est la technique de vélocimétrie par images de particules, qui ne perturbe pas l'écoulement et permet d'obtenir une mesure globale du champ de vitesse. Les simulations sont basées sur un modèle numérique bidimensionnel [4,9] adapté aux écoulements à nombre de Mach faible.

Les visualisations sont obtenues pour deux configurations distinctes. Les paramètres géométriques et ceux de l'écoulement sont listés dans les Tableaux 1 et 2. Les plaques dans la configuration A sont beaucoup plus épaisses que la couche limite visqueuse. Dans la configuration B, l'épaisseur des plaques est presque égale à la couche limite visqueuse. Dans les deux cas, la fréquence de résonance du tube est 200 Hz et l'empilement de plaques est placé à mi-chemin entre un noeud de vitesse et le ventre de vitesse le plus proche de l'extrémité du tube résonnant. Comme indiqué sur la Fig. 1, la fenêtre d'observation de l'écoulement est limitée à l'extrémité froide de l'empilement, où les phénomènes multidimensionels dominent l'écoulement. Dans toutes les figures le noeud de vitesse est situé à gauche de chacune des fenêtres. Dans cette comparaison nous avons pris en compte le fait que les instants de référence utilisés comme origine des temps n'étaient pas identiques entre les expériences et les simulations numériques. Ceci se traduit par un retard d'un seizième de période acoustique entre les données expérimentales et les résultats des simulations numériques. Ce décalage correspond à un déphasage entre le signal d'alimentation de la source acoustique et les oscillations de la pression dans le résonateur. La concordance entre les mesures et les simulations est très satisfaisante.

Comme le montre la Fig. 2, l'écoulement autour de plaques épaisses (configuration A) est dominé par les oscillations de tourbillons denses autour des extrémités des plaques. Ce phénomène s'explique par le détachement de la couche de Stokes caractéristique d'un écoulement dans une telle configuration. Avec la configuration B, les visualisations obtenues (Fig. 3) montrent que le champ de vorticité autour des extrémités des plaques est caractérisé par des couches de vorticités alongées qui s'étendent à l'extérieur du canal et par l'absence de tourbillon au voisinage immédiat des extrémités des plaques. Aux instants où la pression acoustique est maximale ou minimale, l'intensité de la structure vorticale est maximale et la direction de l'écoulement au centre du canal est opposée à celle de l'écoulement le long des plaques. Ce résultat est qualitativement le même que celui prédit par la théorie linéaire, mais une analyse détaillée des profils de vitesse entre deux plaques [8] indique que la théorie linéaire sous-estime l'amplitude du champ de vitesse. Ceci est dû au fait que les effets de bloquage ne sont pas pris en compte dans la théorie analytique. Les résultats obtenus expérimentalement et numériquement sont similaires dans les deux configurations étudiées.

1. Introduction

As schematically illustrated in Fig. 1, a thermoacoustic refrigerator typically comprises a resonance tube that houses a stack of parallel plates, an acoustic source, and heat exchangers (not shown). The operating principle of the device is the well-known thermoacoustic effect [1,2], which results in transport of heat from one end of the stack

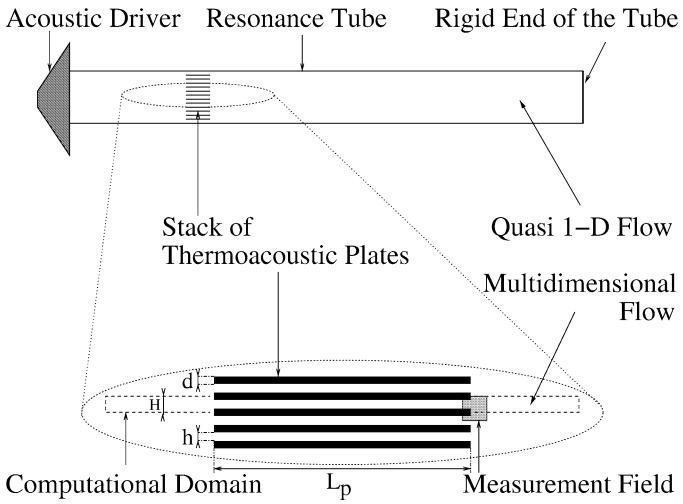

Fig. 1. Schematic illustration of the thermoacoustic refrigerator (top) with a magnified view (bottom) of the computational domain and measurement window.

Fig. 1. Représentation schématique d'un réfrigérateur thermoacoustique (en haut) et vue détaillée du domaine des simulations numériques et de la zone de mesure (en bas).

to the other. By placing hot and cold heat exchangers close to the ends of the stack plates, the thermo-acoustically generated heat flux can be exploited to drive a refrigeration cycle.

Recent computational [3–5] and experimental [6,7] evidence indicates that near the edges of the plates the flow field is dominated by concentrated eddies, whose complex motion significantly affects the performance of the device. Consequently, effective design and optimization of thermoacoustic refrigerators necessitate a fundamental understanding of these vortical motions, and their dependence on geometric parameters and operating conditions.

In this work, quantitative visualization of the unsteady flow field around the edges of a thermoacoustic stack is performed experimentally and computationally. Specifically, time-resolved PIV measurements [8] of the velocity and vorticity fields are compared with computational predictions [9] obtained at similar conditions. We focus on stacks operating at low drive ratios, and present results obtained with two stack configurations that are characterized by disparate ratios of the plate thickness to the viscous penetration depth. As further described below, this enables us to contrast experimental and computational predictions in distinct flow regimes.

2. Experimental setup and approach

The flow field around the stack plates is measured using the particle image velocimetry technique (PIV). PIV is appropriate to visualize flow fields in the resonance tube of thermoacoustic engines since it is a non-intrusive method. It also presents the advantage of providing quantitative information on a global velocity field. The 86 cm-long resonance tube is filled with air and the thermoacoustic stack consists of glass plates. The flow was seeded with small oil droplets of approximately 1 to 2 μm in diameter, generated by a smoke generator located near the acoustic driver. The measurement of the particle velocity was based on two YAG laser sources, where the time delay between two pulses was 40 μs. The light scattered by the seeded particles was recorded by a 1008×1018 Kodak Megaplus E.S. 1.0 camera. Pairs of raw images were cross-correlated using 32×32 pixels interrogation windows, with a 50% overlap ratio between adjacent windows. The data validation is performed by a dynamic procedure using 8 neighbouring points [10]. The PIV measurements were triggered by signals synchronised with the electric supply of the loudspeaker. For a given phase, phase-averaged velocity fields were obtained by averaging 100 instantaneous velocity fields. The whole acoustic cycle was covered by 16 regularly-spaced phases. The measurements are

restricted to a window centered around the cold side of the stack plates, where multi-dimensional phenomena dominate the flow. Using a zooming lens the size of the field of view was 4.2×4.2 mm^2 or 2.9×2.3 mm^2, depending on the spacing between the stack plates. Additional details of the experimental set-up can be found in [8].

3. Numerical model

Simulations of the unsteady flow are performed using a computational model that is an extended version of the scheme originally introduced in [4]. The model relies on a simplified representation of the effect of the resonant standing wave, and on a fully-resolved 2-D representation of the flow in the neighborhood of the stack and heat exchangers. The vorticity-based scheme solves for the compressible conservation equations in the low-Mach-number limit and relies on a physical formulation based on the following assumptions: (1) The Mach number is small and the flow is two-dimensional. (2) The stack is much shorter than the acoustic wavelength. (3) The gas is Newtonian and has constant dynamic viscosity and thermal conductivity. (4) The thickness of the stack plates is very small compared with the gap height and the viscous/thermal penetration depths.

A second-order finite-difference discretization of the equations of motion is used in conjunction with explicit third-order time integration of the discretized evolution equations. The discrete system also includes elliptic equations for the streamfunction and velocity potential, which are efficiently inverted using a specially-tailored domain decomposition approach. This approach enables us to split the original systems into elliptic systems in rectangular subdomains. These subsystems are efficiently inverted using FFT-based Poisson solvers and the overall solution is reconstructed using an influence matrix method.

Computations are performed on a uniform rectangular grid. In order to reduce computational costs, a scheme of successive mesh refinement is implemented. Specifically, extended computations are first performed on a coarse mesh. Once steady state conditions are reached on the coarse mesh, the solution is interpolated on a finer computational grid. This process is repeated until steady state conditions are reached on a grid that is fine enough for quantities to be accurately determined. Data collection over an acoustic cycle starts once steady state is reached on the finest grid. Additional details on the numerical scheme can be found in [9].

4. Results and discussion

As summarized in Tables 1 and 2, two stack configurations are considered in the experiments. In both cases, the center of the stack is located midway between the velocity node and the velocity anti-node, i.e., at a non-dimensional wave-number $kx = \pi/4$. In addition to the geometrical parameters of the stack, the computations use as input the thermal properties of the stack plates and of air, as well as the mean pressure and temperature, respectively $P_m = 10^5$ N/m^2 and $T_m = 300$ K. The experimentally-observed frequency of the resonant standing wave, $f = 200$ Hz is also used as input. Meanwhile, the amplitude of the standing wave is expressed in terms of the drive ratio, Dr, which expresses the ratio of the acoustic pressure amplitude to the mean pressure. The plate Reynolds number Re_d is defined as $u_1 d/\nu$, where u_1 is the peak acoustic velocity at the position of the stack related to the acoustic pressure P_1. We also indicate the peak value of the acoustic displacement ξ.

The two stack configurations are geometrically similar, and are nearly equal in length. However, the thickness and spacing of the stack plates are significantly smaller in configuration B than they are in configuration A. These differences are also highlighted by providing the ratios h/δ_v and d/δ_v, where δ_v is the viscous penetration depth [2]. Thus, d is substantially larger than δ_v in configuration A, but is close to δ_v in configuration B. Accordingly, we shall refer to these two stacks as thick-plate and thin-plate configurations, respectively. The blockage effect of the stacks on the flow is expressed by the blockage ratio $Br = h/(h + d)$.

In both the experiments and computations, data analysis is performed when a "periodically-steady" state is established. This occurs after a large number of acoustic cycles, during which the initial starting transient decays. Once steady state is achieved, instantaneous data on the velocity and vorticity fields is collected at well

Table 1
Geometric parameters for configurations A and B. See Fig. 1 for illustration of symbols

Tableau 1
Paramètres géométriques des configurations A et B. Voir Fig. 1 pour l'illustration des symboles

	d (mm)	h (mm)	L_p (mm)	Br (%)
Configuration A	1.0	2.0	25.8	0.67
Configuration B	0.15	1.0	24.0	0.87

Table 2
Oscillating flow parameters for configurations A and B. See Fig. 1 for illustration of symbols.

Tableau 2
Paramètres de l'écoulement oscillant pour les configurations A et B. Voir Fig. 1 pour l'illustration des symboles

	u_1 (m/s)	ξ (mm)	P_1 (Pa)	Dr (%)	h/δ_ν	d/δ_ν	Re_d
Configuration A	1.71	1.4	707	1.0	13	6.5	119
Configuration B	2.57	2.1	1061	1.5	6.7	1.0	18

defined instants within a single cycle. In both the experiments and computations, 16 equally-spaced, instantaneous realizations are obtained.

In order to perform meaningful comparison between instantaneous realizations, it is necessary to establish a proper synchronization of the time axes. In the experiments, the "phase" is measured with respect to t_0, time at which the (imposed) driving voltage of the acoustic speaker peaks within the cycle. In the computations, on the other hand, the "phase" is measured with respect to t_p, time at which the (imposed) acoustic pressure signal peaks within the acoustic cycle. By performing detailed comparison of the computational and experimental results, we find that closest correspondence occurs when t_p and t_0 are separated by $T/16$ where T is the period of the acoustic cycle. This shift, which is identical for both configurations, suggests a delay between the voltage and pressure oscillations in the experiments. However, this could not be independently verified since the experimental pressure signal at the stack location was not recorded during the PIV measurements. On the other hand, apart from this synchronization of time origins, no adjustments have been performed to either the experimental or computational data.

4.1. Thick-plate configuration

Fig. 2 depicts two instantaneous realizations of the velocity and vorticity fields for configuration A. Shown on the top row are experimental results obtained at $t_0 + T/4$ and $t_0 + 3T/8$; the bottom row depicts computational predictions obtained at $t_p + 3T/16$ and $t_p + 5T/16$. Thus, in both the experiments and computations the two frames are $T/8$ apart. Note that the frame of the computational results has also been restricted to match the 4.2×4.2 mm^2 window of the PIV measurements. As schematically illustrated in Fig. 1, this "test section" is located near the cold-end of the stack plates. In particular, the results are arranged in such a way that the velocity node is located to the left of each frame.

For the present configuration, both the experimental and computational results reveal the presence of concentrated vortices near the edge of the plate. Also evident is the presence of both signs of vorticity, both inside the channel and in the open region. The generation of alternating layers of vorticity within the channel is not surprising, since the ratio of channel height to viscous penetration depth is large and the development of Stokes layers within the channel is accordingly expected. The plate Reynolds number Re_d is also high enough to permit

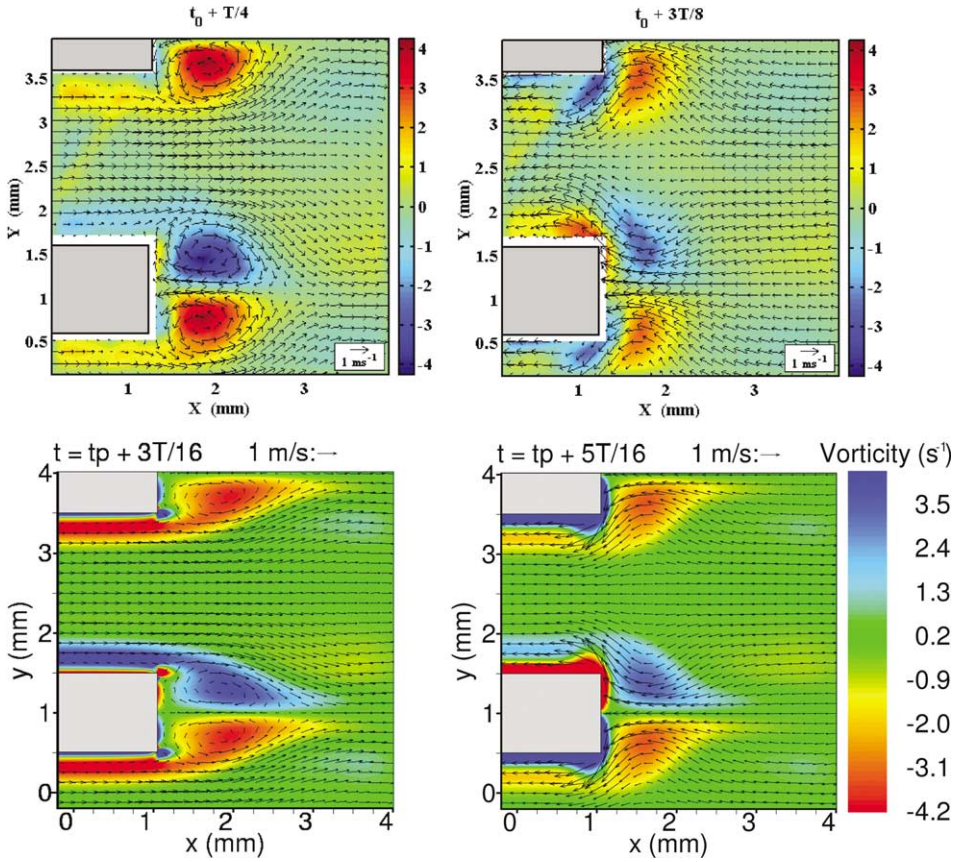

Fig. 2. Instantaneous velocity (vectors) and vorticity (contours) fields around the cold end of the stack in configuration A. Top row: experimental PIV measurements; bottom row: computations. The times at which the frames are generated are indicated in the labels.

Fig. 2. Champs instantanés de vitesse (vecteurs) et de vorticité (contours) au voisinage de l'extrémité froide de l'empilement dans la configuration A. Rangée supérieure : mesures expérimentales obtenues par PIV ; rangée inférieure : simulations. Les instants auxquels les images sont générées sont indiqués pour chaque champ.

the vortex generation. As can be observed in Fig. 2, the vorticity distribution outside the channel can also exhibit complex structure, especially when separated vortices are driven back into the channel and impinge on the edge of the plates.

Comparison of the experimental and computational results in Fig. 2 reveals a close correspondence between the predictions. In particular, at both phases, very good agreement can be observed between peak vorticity values as well as the size of the recirculating regions.

4.2. Thin-plate configuration

Fig. 3 provides computed and experimental results obtained for configuration B. Shown on the left column are computed velocity and vorticity distribution at three selected phases within the cycle; plotted on the right columns are contours of the experimental vorticity distribution at the corresponding times. The figure is generated in a similar fashion as in Fig. 2, i.e., the computational test section is restricted so that it matches the experimental window. In the present case, the PIV measurements are performed in a 2.9×2.3 mm^2 window, also located near the cold end of the stack.

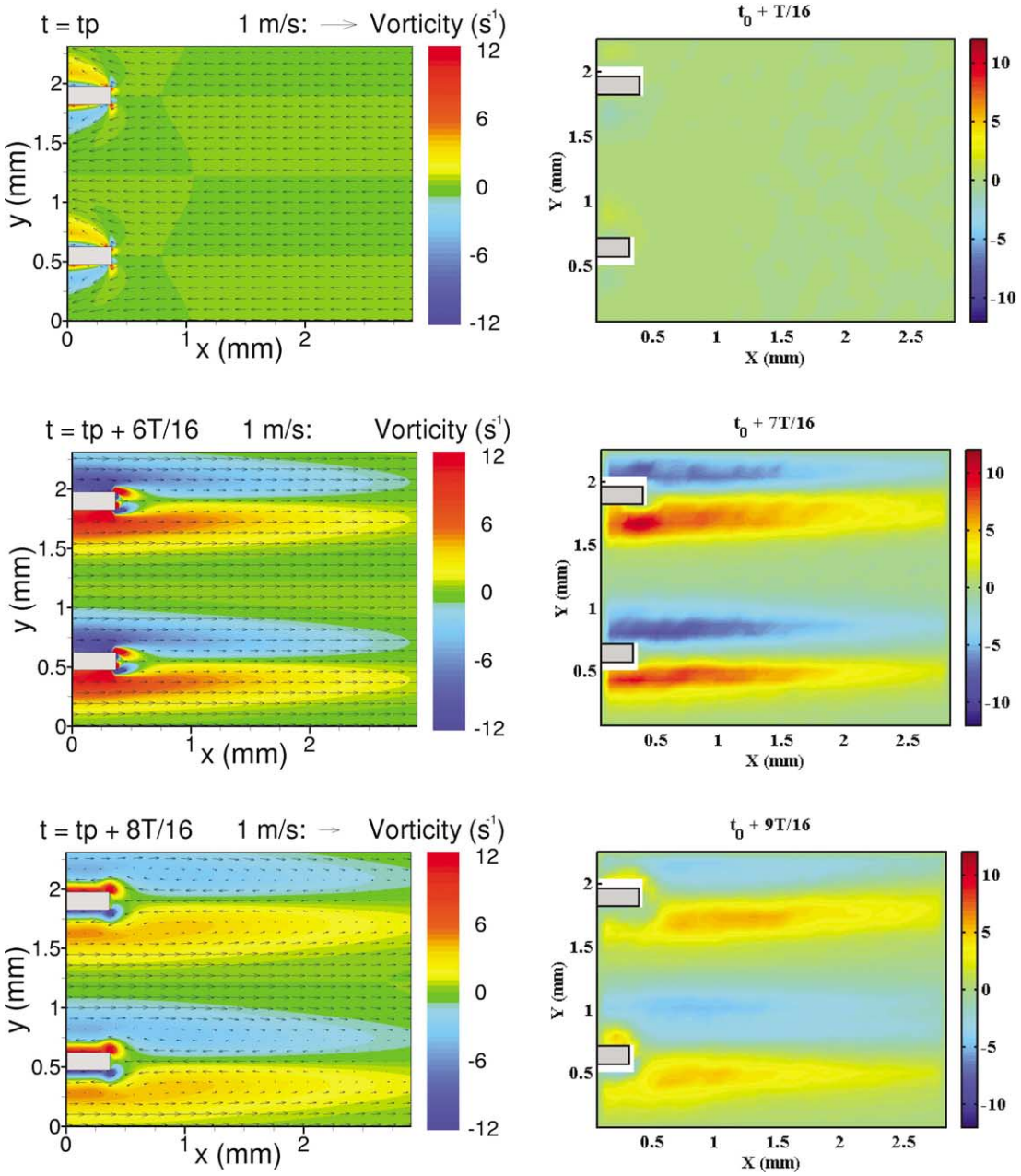

Fig. 3. Left: Computed velocity (vectors) and vorticity (contours) fields at selected times for configuration B. Right: instantaneous vorticity contours from PIV measurements. The times at which the frames are generated are indicated in the labels.

Fig. 3. À gauche : Champs de vitesse (vecteurs) et de vorticité (contours) à des instants choisis obtenus par simulation dans la configuration B. À droite : champs instantanés de vorticité obtenus par PIV. Les instants auxquels les images sont générées sont indiqués pour chaque champ.

The present predictions are in sharp contrast with the observations of case A. Specifically, in the present case B the results do not show the formation of well-defined eddies. The vorticity distribution in the wake exhibits the presence of elongated layers that extend well outside the channel. However, significant rollup of these layers is not observed, although evidence of very weak recirculating motion near the plate corners can be detected in the last computational frame.

Note that the top and bottom frames in Fig. 3 correspond to t_p and $t_p + T/2$, times at which the acoustic pressure is maximal and minimal, respectively. At these phases, the streamwise extent of the vortical wake, is found to be maximal and the direction of the flow in the middle of the channel is opposite to that of the flow along the plate surface. The computed and measured velocities are in good agreement with each other. As noted by Duffourd [8], the measured velocities are slightly larger than the velocity profiles derived using the linear theory [2,11] for the same configuration. As discussed in [3], this discrepancy is most likely due to blockage effects which are ignored by the linear theory.

5. Conclusions

Visualization of the flow field in a thermoacoustic stack has been performed experimentally using PIV measurements and computationally using a low-Mach-number model. Two stack configurations at different drive ratios are included in the study. For both configurations, computational and experimental results on instantaneous velocity and vorticity fields are found to be in close agreement; this provides strong support to both approaches. Extension of the combined analysis to high-drive-ratio regimes is currently being planned.

Acknowledgements

The work of EB and OK was supported by the Office of Naval Research. The visit of PhBB to The Johns Hopkins University was supported by ONRIFO. Computations were performed at the National Center for Supercomputing Applications. Experiments was supported by Délégation Générale à l'Armement under contract number DSP N° 97-2532. PhBB also thanks M. Michard, Ch. Nicot and N. Grosjean for their contributions.

References

[1] Lord Rayleigh, Theory of Sound, Dover, New York, 1945.
[2] G.W. Swift, Thermoacoustic engines, J. Acoust. Soc. Am. 84 (1988) 1145–1180.
[3] A.S. Worlikar, O.M. Knio, Numerical simulation of a thermoacoustic refrigerator. Part I: Unsteady adiabatic flow around the stack, J. Comput. Phys. 127 (1996) 424–451.
[4] A.S. Worlikar, O.M. Knio, R. Klein, Numerical simulation of thermoacoustic refrigerator. Part II: Stratified flow around the stack, J. Comput. Phys. 144 (1998) 299–324.
[5] A.S. Worlikar, O.M. Knio, Numerical study of oscillatory flow and heat transfer in a loaded thermoacoustic stack, Numer. Heat Transfer Part A 35 (1999) 49–65.
[6] M. Wetzel, C. Herman, Experimental study of thermoacoustic effects on a single plate. Part II: Heat transfer, Heat Mass Transfer 35 (1999) 433–441.
[7] M. Wetzel, C. Herman, Experimental study of thermoacoustic effects on a single plate. Part I: Temperature fields, Heat Mass Transfer 36 (2000) 7–20.
[8] S. Duffourd, Réfrigérateur Thermoacoustique: Études analytiques et expérimentales en vue d'une miniaturisation, Ph.D. Thesis, N°2001-06, École Centrale de Lyon, 2001.
[9] E. Besnoin, Numerical Study of Thermoacoustic Heat Exchangers, Ph.D. Thesis, Department of Mechanical Engineering, The Johns Hopkins University, 2001.
[10] M. Raffel, C. Willert, J. Kompenhans, Particle Image Velocimetry. A Practical Guide, Springer-Verlag, Berlin, 1998.
[11] W.P. Arnott, H. Bass, R. Raspet, General formulation of thermoacoustics for stacks having arbitrarily shaped pore cross sections, J. Acoust. Soc. Am. 90 (1991) 3228–3237.